Nanoscale Advances

ROYAL SOCIETY OF CHEMISTRY

PAPER

View Article Online
View Journal

Cite this: DOI: 10.1039/d5na01063b

Performance improvement of an Au and TiO_2 coated D-shaped photonic crystal fiber (PCF) based SPR sensor for cancer detection

Kazi Zannatul Ferdwushee, Md Abu Shahid Chowdhury * and Siddika Tamanna Islam

Surface plasmon resonance (SPR) has been an emerging tool for the recognition of cancer in a label-free manner. However, conventional SPR setups are based on prism coupling, which makes them bulky, hindering their capability to be integrated into compact and portable devices. To overcome these issues, the proposed approach introduces a photonic crystal fiber (PCF) structure with a micro-channel D-shaped, integrated with a gold (Au) coating as the plasmonic substance and titanium dioxide (TiO_2) as a dielectric substance. It minimizes the distance of the plasmonic film from the fiber core, thus elevating the sensor performance. In addition, the introduction of TiO_2 over the plasmonic film alters the plasmon–analyte interaction, thus increasing the sensitivity. The numerical simulation for the designed sensor is done in COMSOL Multiphysics software through the finite element method (FEM). After optimization, the sensor is numerically evaluated for the identification of six various carcinoma cell types for refractive indices between 1.360 to 1.401. The ultimate achieved amplitude and spectral sensitivities are 717.29 per RIU and 7142.86 nm per RIU, respectively, recorded for MDA-MB-231 and MCF-7 cells. Additionally, the optimized sensor can distinguish a diverse array of biomolecules across the RI span of 1.330 to 1.420, attaining a peak spectral sensitivity of 20 000 nm per RIU for *y*-polarized light. Moving further, the sensor also delineated excellent figure of merit, resolution, and amplitude sensitivity values of 366 per RIU, 5×10^{-6} RIU, and 1178 per RIU, respectively, within the mentioned RI domain. The measured outcomes show that the designed sensor could be a potential option for the precise identification of various cancer cells.

Received 14th November 2025
Accepted 28th May 2026

DOI: 10.1039/d5na01063b

rsc.li/nanoscale-advances

1. Introduction

A total number of 618 120 cancer fatalities and 2 041 910 newly discovered carcinoma cases are estimated to occur in the USA by the end of 2025.[1–4] The global death toll projection is going up to 16.9 million per year by the year 2045. A significant portion of cancers exhibit no symptoms until later stages, demonstrating the disease's complex and challenging nature, with 70% of cancer fatalities in resource-limited areas resulting from restricted access to early screening and treatment.[5] Despite significant advances in conventional cancer detection methods, such as imaging modalities like mammography, MR imaging, computed tomography (CT), positron emission tomography (PET), and biopsies, as well as blood and tissue-based diagnostic evaluation tools like polymerase chain reaction (PCR) and enzyme-linked immunosorbent assay (ELISA), these mechanisms still endure major drawbacks. These include low specificity, high costs, radiation exposure risk, time-intensive procedures, and dependency on advanced laboratory setup, among others.[6] While AI and machine learning have contributed to improved scan accuracy, these technologies still do not provide the kind of non-invasive, real-time, and universal cancer detection needed.[7] Taking into consideration the significant constraints that the traditional methods present, it is logical to say that the healthcare system needs quick, inexpensive, and non-invasive diagnostic alternatives. A biosensor could be a probable solution for overcoming the aforementioned limitations due to its sensitive, selective, and time-efficient analysis of biological targets in a user-friendly manner. Present-day biosensors use enzymes and antibodies as biorecognition elements in their detection of cancer biomarkers.[8,9] However, the use of enzymes and antibodies results in degradation over time, and subsequently, the sensor performance is affected.

In this context, optical biosensors can hold significant potential in cancer diagnosis owing to their real-time and continuous detection in a highly responsive, selective, affordable, and non-invasive manner. Different optical biosensors also have dependence on labeled techniques, which incorporate electrochemically active probes, fluorescent labeling, and chemiluminescence. Nevertheless, this method can be quite

Department of Biomedical Engineering, Khulna University of Engineering & Technology, Khulna, 9203, Bangladesh. E-mail: shahid@bme.kuet.ac.bd

expensive, require a lot of time, and may also disrupt the receptor–analyte interactions.[10] To avoid this problem, label-free optical sensors are strongly recommended. Surface plasmon resonance (SPR) biosensors that allow the identification of target substances at very low concentrations without the need for labeling are the most precise optical methods.[11,12] The SPR serves as a powerful tool for point-of-care testing of oncogenic biomarkers in a label-free manner with high specificity, sensitivity, fast sensing, and high repeatability, which can also characterize distinct types of carcinomas. The principle behind the SPR biosensor is a shift in the refractive index (RI) in the ambient environment being measured as it relates to the binding of molecules at the surface of the metal. A hetero-structured SPR biosensor composed of graphene and MXene ($Ti_3C_2T_X$), along with a BK7 prism, gold (Au), and aluminum oxide (Al_2O_3) for the rapid characterization of a well-known cancer-associated marker, carcinoembryonic antigen, was proposed by Khodaie and Heidarzadeh.[13] The findings presented a figure of merit (FoM) of 17.52 per RIU and a comparatively enhanced sensitivity of 163.63 deg per RIU. The use of ZnO and TMDC layers in a SPR biosensor by Jiang *et al.*[11] allowed for the identification of distinct carcinoma cells. The proposed biosensor demonstrated the figure of merit and the highest sensitivity values of 124.86 per RIU and 342.14 deg per RIU in terms of detecting blood cancer (Jurkat) cells from healthy cells. Another recent study proposed a $BaTiO_3$ and black phosphorus-based SPR biosensor for the identification of different malignancy biomarkers, where a maximum sensitivity of 417.86 deg per RIU was achieved for breast cancer MCF-7 cells (mammary carcinoma type II).[5] On the other hand, the regular prism-coupled SPR setups, which are the basis for sensing technologies, have some drawbacks, such as their large size, high price, and the fact that they are difficult to incorporate into small, portable devices.

In this context, the fiber optic SPR sensors, particularly those utilizing photonic crystal fiber (PCF), so to speak, are the ones bringing the solution to the problems because they are providing miniaturized, flexible, and robust platforms that are, at the same time compatible with *in vivo* applications and point-of-care diagnostics.[14] These enticing features make PCF-based SPR sensors desirable for various biosensing applications, including the detection of blood components,[15] heavy metals,[16] cancer cells,[17] and various other diseases.[18] Additionally, the use of AI for geometrical optimization has further enhanced the potential of PCF-based SPR sensors for biomedical applications.[19] Among various fiber geometries, including circular, D-shaped, slotted, and bowl-shaped, the D-shaped structure can improve sensor performance by incorporating micro-channels.[20,21] Numerous researchers have reported a wide variety of D-shaped structures for detecting various analytes. For instance, Divya *et al.*[22] suggested a dual-channel D-shaped PCF-based plasmonic sensor that is able to sense two different analytes simultaneously. The sensor went through an optimization process and then reached the peak amplitude and wavelength sensitivities of 216 per RIU and 10 000 nm per RIU, respectively. Another research work reported by Zhou *et al.*[23] was on a D-shaped PCF-based SPR sensor whose core was an open-ring channel sandwiched between a gold deposition to trigger the plasmonic modes. They showed that analyte placement significantly affects sensitivity. Specifically, when the target analyte was positioned across the outer ring structure, the sensor exhibited an RI finding that lies within the span of 1.2 to 1.34, achieving a peak sensitivity of 2000 nm per RIU. In contrast, when the analyte was placed only on the open channel, the measurable RI span extended from 1.33 to 1.46, and the sensor achieved a peak sensitivity of 5600 nm per RIU. To further improve the performance, Oudenani and Sonne proposed a D-shaped SPR-Based PCF biosensor, which obtained optimum amplitude sensitivity (AS) and wavelength sensitivity (WS) values of 1623.6 per RIU and 12 300 nm per RIU, respectively.[24] Moving further, Azadi *et al.*[25] conducted a study wherein a TiO_2 dielectric coating was incorporated between a gold plasmonic layer and silica. This structure achieved an optimized AS of 610 per RIU and WS of 14 000 nm per RIU. Moreover, the D-shaped design is efficacious in terms of production as it does not require a complicated setup, as in the case of circular or dual-core PCF, besides being more durable with the Au or TiO_2 coatings, and allowing dual-polarization for further deterring of non-target interfering molecules with increased specificity.[13]

Such facts have prompted this study to go for a D-shaped sensor, which facilitates enhanced performance in distinguishing between different cancer cells and their normal counterparts. The FEM is used to develop and investigate the designed sensor. The study critically examined how the orientation of air spaces, their diameter, and the height of the plasmonic film and overlayers affected the overall effectiveness of the sensor. The influence of the open channel on sensor efficacy is also evaluated. After a thorough study and evaluation, it is concluded that the adjusted sensor structure can identify six different cancer biomarkers from the corresponding healthy cells with maximum AS and WS of 717.29 per RIU and 7142.86 nm per RIU, respectively, for MDA-MB-231 and MCF-7 cells. In addition, the optimized sensor exhibited maximum sensitivities, figure of merit, and resolution values of 20 000 nm per RIU, 1178 per RIU, 366 per RIU, and 5×10^{-6} RIU, respectively, within a wide RI span from 1.330 to 1.420 for *y*-polarized light. This depicts the sensor's effectiveness in detecting a broad spectrum of bioanalytes with enhanced performance, illustrating its potential to be a strong tool for medical diagnostics.

2. Design of PCF structure and theoretical model

2.1. Overview of the PCF framework

This study describes the design and numerical assessment of a SPR sensor based on PCF, utilizing the full-vector FEM in COMSOL Multiphysics 6.1. Fig. 1a and b depict the schematics of the designed structure and finite element mesh. Simulations were conducted using a frequency-domain eigenmode solver with a non-uniform triangular mesh. A non-uniform triangular mesh with local refinement at the Au and Au–TiO_2 interface

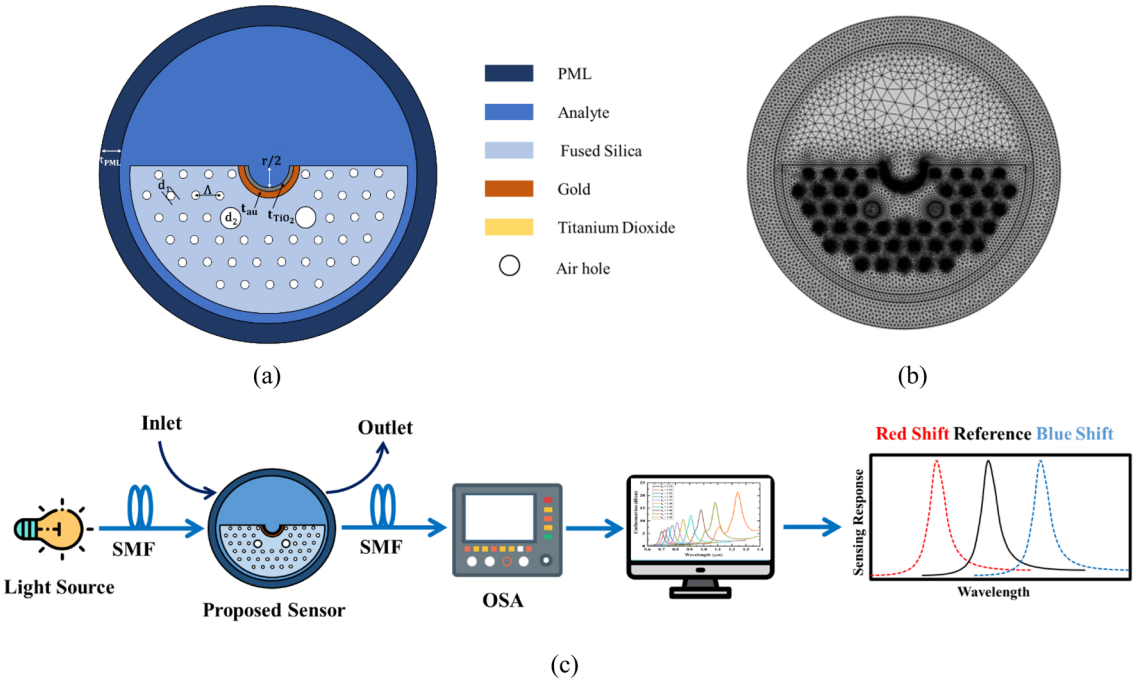

Fig. 1 Cross-sectional view of the (a) designed microchannel-type D-shaped sensor, (b) finite element mesh, and (c) experimental setup of the proposed sensor.

(192 032 domain, 6136 boundary elements) ensured convergence. Electromagnetic boundary conditions included PML at domain edges, and continuity at material interfaces was implemented. Effective index and confinement loss were extracted from Im(n_{eff}) using default solver tolerances. The sensor comprises three main components: a silica (SiO_2) substrate featuring circular air holes organized in a hexagonal lattice, a gold (Au) plasmonic layer, and an analyte channel. The cladding region comprises two separate types of air holes, labeled d_1 and d_2, meticulously designed for superior optical confinement and improved sensing efficacy. The midpoint-to-midpoint gap between neighboring air holes is labeled as pitch (Λ), which determines the modal properties and the guided mode's effective refractive index. A thin coating of TiO_2 is embedded between the Au layer and the analyte with a height of t_{TiO_2}. After conducting a series of optimization experiments, the structural parameters have been established as pitch = 4 μm, $r = 8$ μm, $d_1 = 1.1$ μm, $d_2 = 3$ μm, $t_{au} = 55$ nm, and $t_{TiO_2} = 9$ nm. t_{au} indicates the height of the Au. The D-shaped arrangement is attained by polishing the fiber surface near the core region, which minimizes the separation between the guided core mode and the Au plasmonic layer. This reduced distance enhances the penetration of the evanescent electric field into the plasmonic coating interface, increasing the modal overlap and improving phase matching with the SPP mode, thereby strengthening SPR excitation and excitation efficiency. The external section of the structure includes an analyte open microchannel with diameter r and a perfectly matched layer (PML) with a thickness of $t_{PML} = 5$ μm, to mitigate undesirable boundary reflections.

Fig. 1c explains a simplified representation of the experimental setting for the sensing approach, including an optical tunable source (OTS) and an optical spectrum analyzer (OSA). The designed sensor is interconnected *via* a single-mode fiber (SMF). The analyte is placed on the external surface of the sensor, which can be regulated using a pump that passes through the IN/OUT channel. The interaction between the unknown analyte and the sensor surface produces a resonance wavelength shift toward the red or a blue shift, as depicted in Fig. 1c. The OSA can monitor this phenomenon. The unidentified analyte can be determined by investigating the confinement loss on a computer.

2.2. Material selection and theoretical basis

Gold (Au) is an effective plasmonic substance due to its remarkable chemical stability, biocompatibility, and extensive plasmon resonance bandwidth, rendering it highly appropriate for sensing applications. The relative dielectric properties of Au are delineated by the Drude–Lorentz model.[26]

$$\varepsilon_{Au}(\omega) = \varepsilon_{\infty} - \frac{{\omega_D}^2}{\omega(\omega + i\gamma_D)} - \frac{\nabla\varepsilon \cdot {\Omega_L}^2}{\left({\omega^2} - {\Omega_L}^2\right) + i\Gamma_L\omega} \quad (1)$$

where ε_{Au}, ε_{∞}, ω_D, γ_D, Γ_L, ∇_{ε}, and Ω_L are the relative dielectric properties of Au, the high-frequency dielectric property, the plasmon frequency, the damping coefficient, the frequency bandwidth of the Lorentz oscillators, the weighted parameter, and the oscillator strength, respectively, with their values specified in Table 1.

A thin TiO_2 layer is applied as an optical tuning material on the Au coating to modify the local dielectric conditions at the

Table 1 Drude–Lorentz model parameters

ε_∞	$\omega_D/2\pi$ (THz)	$\gamma_D/2\pi$ (THz)	$\Gamma_L/2\pi$ (THz)	$\Omega_L/2\pi$ (THz)	$\nabla\varepsilon$
5.96730	2113.60	15.920	104.86	650.07	1.09

Table 2 Sellmeier dispersion parameters

E_1	E_2	E_3	F_1	F_2	F_3
0.6961663	0.4079426	0.8974794	0.0684043	0.1162414	9.896161

metal–dielectric interface. Its high RI enhances electromagnetic field confinement and improves phase matching with the surface plasmon polariton (SPP) mode, leading to stronger plasmon–analyte interaction and improved RI sensitivity. The subsequent equation determines the relation between the wavelength of TiO_2 and its RI.[27]

$$n_{TiO_2}{}^2 = 5.913 + \frac{2.441 \times 10^7}{(Wl^2 - 0.803 \times 10^7)} \quad (2)$$

In this context, Wl denotes the operational wavelength in angstroms, and the titanium dioxide's RI is n_{TiO_2}.

Fused silica serves as the foundational substance of the structure in this research. The RI of fused silica changes with the wavelength of light, which causes material dispersion when the fiber is in operation. Therefore, it is fundamental to perform numerical simulations to assess how material dispersion affects the PCF's transmission properties. The Sellmeier equation can determine the RI of fused silica.[28]

$$n^2(Wl) = 1 + \frac{E_1 Wl^2}{Wl^2 - F_1{}^2} + \frac{E_2 Wl^2}{Wl^2 - F_2{}^2} + \frac{E_3 Wl^2}{Wl^2 - F_3{}^2} \quad (3)$$

where the RI is denoted as n, and Wl is the wavelength of fused silica, measured in microns. The dispersion parameters of the Sellmeier equation are given in Table 2.

The assessment of sensing performance in PCF-based SPR sensors is significantly dependent on the analysis of confinement loss. The subsequent formula can be used to determine the confinement loss.[29]

$$\alpha(\text{dB cm}^{-1}) = 8.686 \times 10^4 \times \left(\frac{2\pi}{Wl}\right) \times \text{Im}(n_{\text{eff}}) \quad (4)$$

where $\text{Im}(n_{\text{eff}})$ and Wl denote the fictitious segment of the effective RI, and the incident wavelength, respectively.

The wavelength sensitivity (WS) analysis is a key parameter to assess the sensor's performance. The spectral interrogation approach evaluates sensitivity by observing the shift in resonance wavelength relative to the analyte's RI, mathematically represented as follows.[30]

$$WS = \frac{\Delta Wl_{\text{peak}}}{\Delta n_a} \text{ (nm per RIU)} \quad (5)$$

The shift in resonance wavelength, which occurs between two successive peaks, is represented by ΔWl_{peak} and the difference between the two RIs is represented by Δn_a.

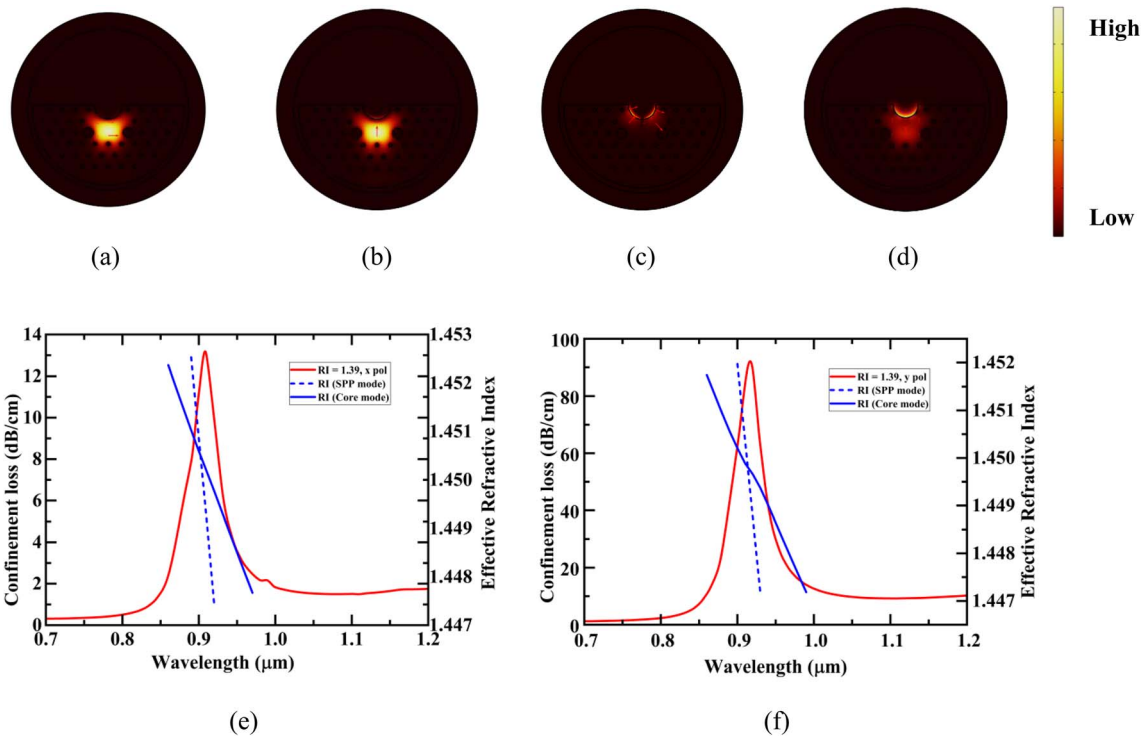

Fig. 2 The electric field profile of (a and b) the fundamental core mode and (b and c) the SPP mode, and dispersion curve of (e and f) confinement loss, fundamental mode, and SPP mode of $n_a = 1.39$, transverse polarizations (x and y), respectively.

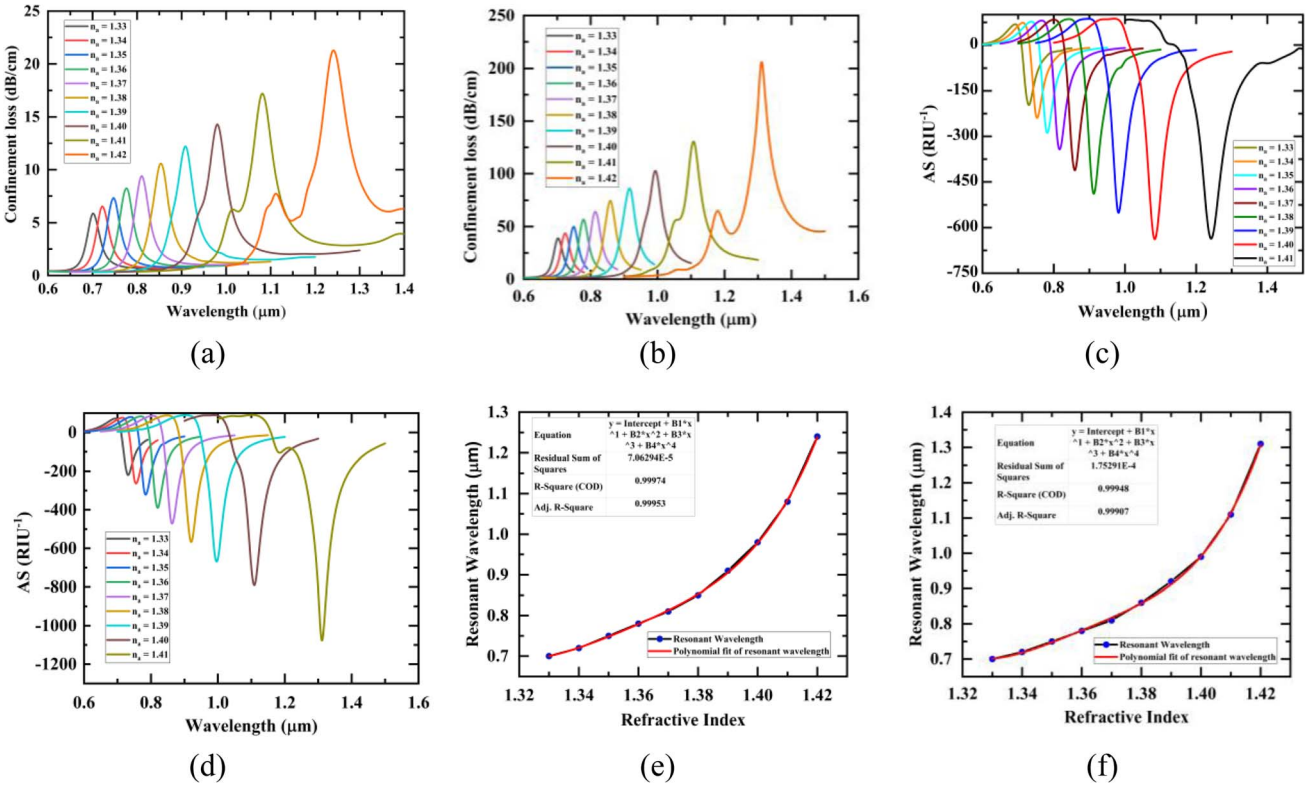

Fig. 3 Dispersion profile of (a and b) confinement loss, (c and d) AS, and (e and f) fitting polynomials to the resonance wavelengths for an analyte RI variation from 1.33 to 1.42 for transverse polarizations (*x* and *y*), respectively.

The sensor performance can be evaluated by another significant measurement called amplitude sensitivity (AS). AS depends on variations in oscillatory strength and recognizes the analyte by assessing the changes in confinement loss. The formula for measuring AS is presented as follows:[31]

$$\mathrm{AS(Wl)} = -\frac{1}{\alpha(\mathrm{Wl}, n_a)} \times \frac{\partial\alpha(\mathrm{Wl}, n_a)}{\partial n_a} (\text{per RIU}) \quad (6)$$

The variation in confinement loss between two analytes is $\partial\alpha(\mathrm{Wl},n_a)$, and confinement loss for the analyte used for the detection is $\alpha(\mathrm{Wl},n_a)$. Within this context, ∂n_a denotes the change between the RIs of analytes that are adjacent.

Furthermore, the sensor's figure of merit (FoM) is evaluated to assess the sensing efficacy. The FoM is a quantitative indicator that tells the effectiveness of a sensor, with higher values indicating a higher degree of precision for identifying the RI of a solution. The subsequent equation can be applied to express the FoM.[32]

$$\mathrm{FoM} = \frac{\mathrm{WS}}{\mathrm{FWHM}} (\text{per RIU}) \quad (7)$$

In this context, WS signifies the wavelength sensitivity, and FWHM refers to the full width at half maximum, indicating the width of the loss spectrum at half of its peak value.

Sensor resolution delineates the sensor's capability to perceive deviations in the analyte's RI. This determination is conducted utilizing the following equation:[33]

$$R = \Delta n_a \times \frac{\Delta \mathrm{Wl}_{\min}}{\Delta \mathrm{Wl}_{\mathrm{peak}}} (\mathrm{RIU}) \quad (8)$$

where, R is the sensor resolution, and $\Delta\mathrm{Wl}_{\min}$ represents the smallest possible wavelength resolution.

3. Simulation results and discussion

3.1. Quantitative findings and sensitivity evaluation

The evanescent electromagnetic field induced by light traveling within the fiber core is essential in a PCF-based SPR sensor, as it

Table 3 Assessment of sensor performance for AS and WS over different analyte RI variations

Analyte RI	Resonant wavelength (nm)		WS (nm per RIU)		AS (per RIU)		FoM (per RIU)	
	x-pol	*y*-pol	*x*-pol	*y*-pol	*x*-pol	*y*-pol	*x*-pol	*y*-pol
1.33	700	700	2000	2000	219	247	66	68
1.34	720	720	3000	3000	265	278	97	99
1.35	750	750	3000	3000	322	346	92	97
1.36	780	780	3000	3000	354	429	87	92
1.37	810	810	4000	5000	445	508	109	142
1.38	850	860	6000	6000	526	615	144	155
1.39	910	920	7000	7000	594	688	149	152
1.4	980	990	10 000	12 000	658	836	197	215
1.41	1080	1110	16 000	20 000	653	1178	265	366
1.42	1240	1310						

Table 4 A comparative study of the proposed D-shaped PCF-based SPR sensor's performance with recently reported PCF-based SPR sensors

Configuration	RI range	Max. WS (nm per RIU)	Max. AS (per RIU)	R (RIU)	FoM (per RIU)	Ref.
Dual-channel D-shaped	1.31–1.41	10 000	216	5×10^{-5}	125	36
D-shaped	1.35–1.46	5600	—	8×10^{-4}	—	37
D-shaped	1.26–1.38	5400	—	—	—	38
Hoop-cut	1.39–1.44	2000	374.062			39
Proposed structure	1.33–1.42	20 000	1178	5×10^{-6}	366	

interacts with electrons on the plasmonic film and enables the excitation of a surface plasmon wave. The optical field is confined and propagates along the core region during light transmission, while the SPP mode is generated at the sensing zone, where the plasmonic coating and overlayer are introduced. The operational characteristics depend on the integration of the core mode with the SPP mode. As the first step, we examine the evanescent electromagnetic field profile, which shows a significant coupling between the fundamental mode and the SPP mode for both transverse polarizations (x and y), as presented in Fig. 2a–d.

Fig. 2e and f show that, for both transverse polarizations (x and y), the plasmonic layer can excite the SPP mode within a certain wavelength range and resonantly interact with the fundamental mode at different frequencies. For x- and y-polarizations, the loss peaks appear at wavelengths of 910 nm and 920 nm, with corresponding confinement losses of 12.95 dB cm^{-1} and 89.21 dB cm^{-1}, respectively. Overall, y-polarization yields a sharper peak profile and a higher loss peak. This indicates that the plasmonic resonance state is more noticeable in y-polarization and that the SPP mode is excited more effectively.

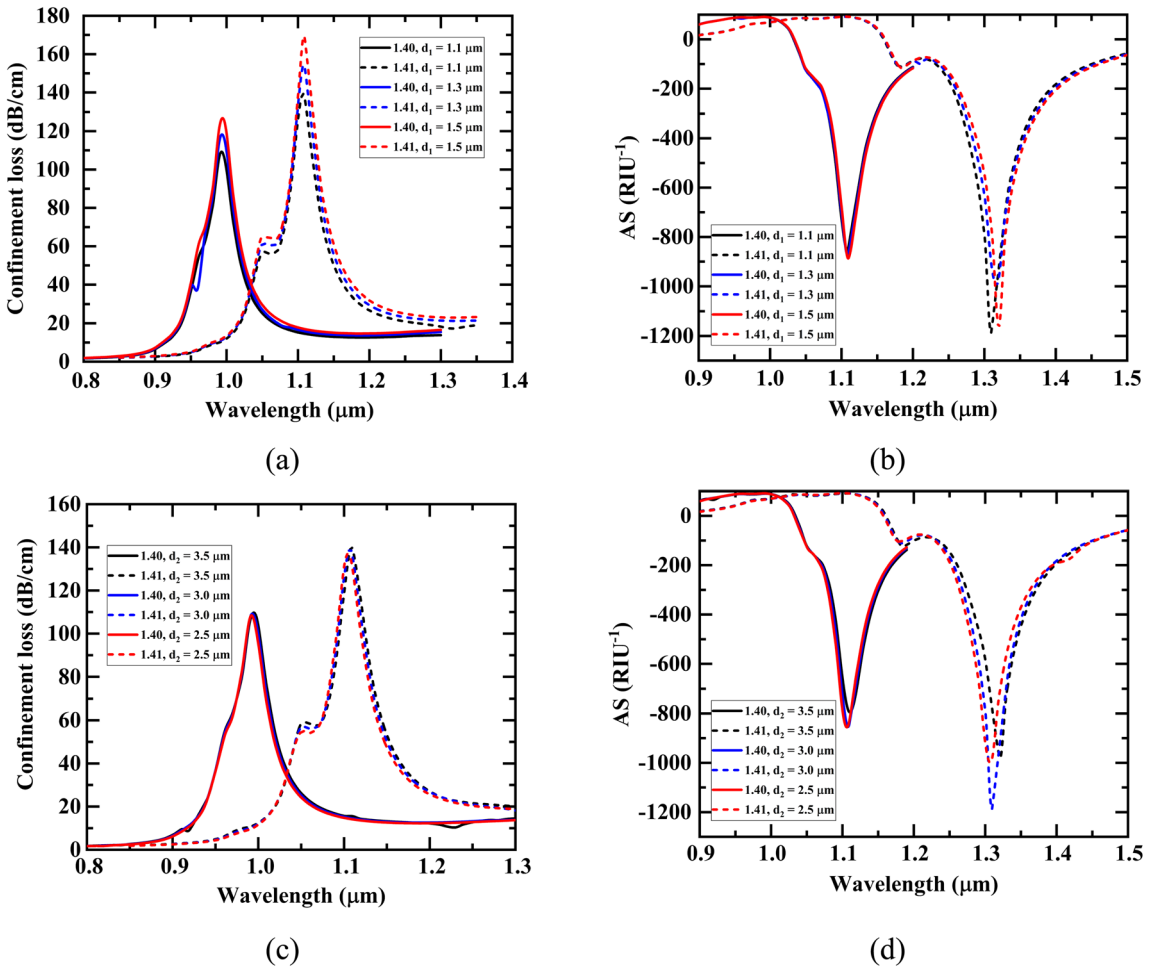

Fig. 4 Effect of the variation in air hole diameters d_1 and d_2 on the sensor's (a and c) confinement loss, and (b and d) AS for analyte RI varying from 1.40 to 1.41, respectively.

Table 5 The optimized values of geometric parameters for analyte RI detection range from 1.40 to 1.41

Diameter (μm)	Wl_{peak} (μm), $n_a = 1.40$	Wl_{peak} (μm), $n_a = 1.41$	Confinement loss (dB cm^{-1}), $n_a = 1.40$	Confinement loss (dB cm^{-1}), $n_a = 1.41$	AS (per RIU), $n_a = 1.40$	AS (per RIU), $n_a = 1.41$
d_1						
1.1	0.99	1.11	106.88	135.83	836	1178
1.3	0.99	1.11	114.95	151.69	862	971
1.5	0.99	1.11	122.12	166.71	885	1164
d_2						
3.5	0.99	1.11	105.41	139.10	795	977
3	0.99	1.11	106.88	135.83	836	1178
2.5	0.99	1.1	107.06	130.99	824	977
r						
8	0.99	1.11	106.88	135.83	836	1178
7	0.98	1.09	88.59	114.80	838	958
6	0.97	1.07	74.79	93.42	826	913
Pitch (μm)						
3.8	1.00	1.11	141.45	182.23	842	875
4.0	0.99	1.11	106.88	135.83	836	1178
4.2	0.99	1.10	84.98	105.51	808	848

Since the majority of chemical sensing processes and biochemical interactions usually occur within the RI ranging from 1.33 to 1.42, this range is chosen for investigation.[34,35] As the analyte RI fluctuates between 1.33 and 1.42, Fig. 3a and b display the confinement loss characteristics for both transverse polarizations (x and y), which are used to evaluate the sensor's

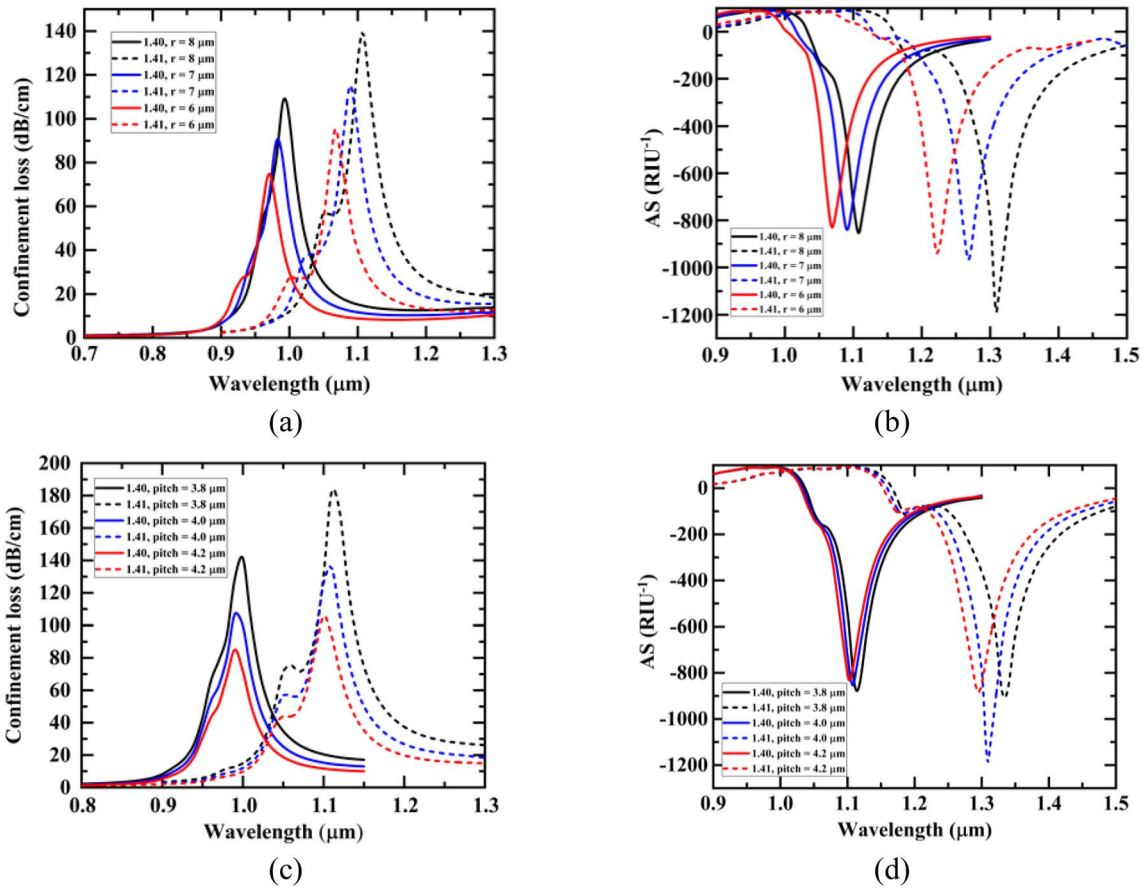

Fig. 5 Effect of the variation in microchannel diameter r and pitch distance on the sensor's (a and c) confinement loss, and (b and d) AS for analyte RI varying from 1.40 to 1.41, respectively.

Table 6 A thorough explanation of the correlation between the Au and TiO_2 layer height with sensor sensitivity

Material thickness (nm)	Wl_{peak} (μm), $n_a = 1.40$	Wl_{peak} (μm), $n_a = 1.41$	Confinement loss (dB cm^{-1}), $n_a = 1.40$	Confinement loss (dB cm^{-1}), $n_a = 1.41$	AS (per RIU), $n_a = 1.40$	AS (per RIU), $n_a = 1.41$
Au						
60	1.0	1.11	70.33	85.68	613	649
55	0.99	1.11	106.89	135.83	836	1178
50	0.99	1.10	173.75	274.77	1405	1100
TiO_2						
10	1.02	1.13	110.60	141.70	798	1243
9	0.99	1.11	106.87	135.83	836	1178
8	0.97	1.08	104.43	133.22	852	1050

efficiency for multiple analytes. Increasing RI of the analyte induces the resonance peak to redshift toward higher wavelengths, as shown in Fig. 3a and b. A slight change in the RI of the analyte influences the plasmonic mode's RI, which in turn shifts the phase-matching position. When the analyte RI changes from 1.41 to 1.42, the resonance wavelength exhibits maximum shifts of 160 nm and 200 nm for transverse polarizations (x and y), respectively. The optimal WSs achieved at RI = 1.41 of 16 000 nm per RIU and 20 000 nm per RIU for the transverse polarizations (x and y) modes, respectively.

The effectiveness of the sensor is further evaluated by determining AS using the amplitude measurement approach

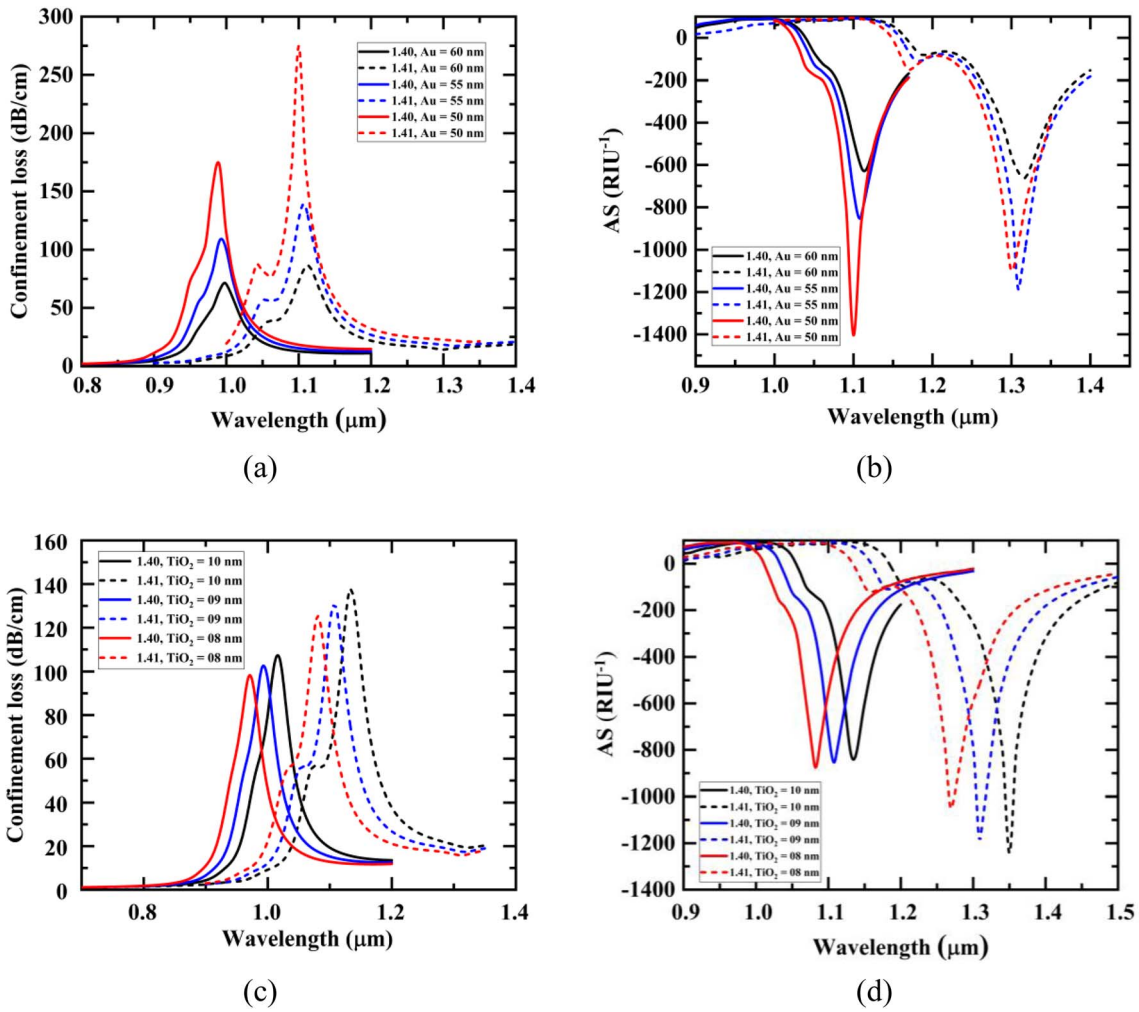

Fig. 6 Impact of the variation in Au and TiO_2 layer thickness on the sensor's (a and c) confinement loss, and (b and d) AS for analyte RI varying from 1.40 to 1.41, respectively.

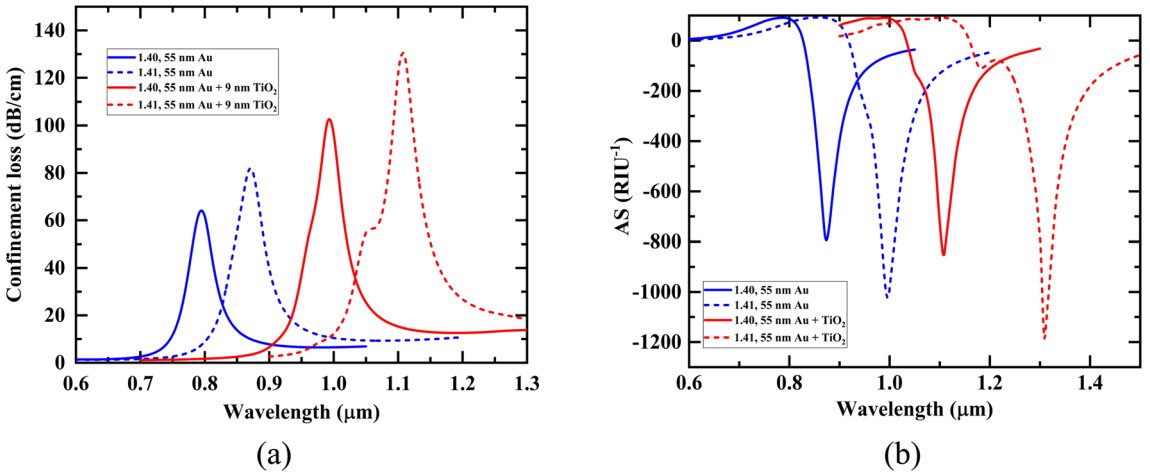

Fig. 7 Dispersion profile of (a) confinement loss and (b) AS for analyte RI varied from 1.40 to 1.41, when the simulation uses only an Au layer and with a TiO_2 overlayer.

for both transverse polarizations (x and y), as displayed in Fig. 3c and d. The y-polarization mode demonstrates greater performance (AS) than the x-polarization mode, due to a more pronounced loss peak observed in the y-polarization response. The peak ASs of 658 per RIU and 1178 per RIU are measured for the transverse polarizations (x and y) modes, respectively.

The sensor's performance is quantified using the figure of merit (FoM). A higher FoM signifies superior sensor performance. The estimated FoM values for various analyte RIs are presented in Table 3. The designed sensor obtains a maximum FoM of 265 and 366 per RIU for transverse polarization modes (x and y), respectively. Along with sensitivity and FoM, the resolution (R) of the designed sensor is evaluated to provide an in-depth assessment of its performance. The maximum resolutions of 6.25×10^{-6} and 5×10^{-6} RIU are observed for the transverse polarization modes (x and y), respectively.

The efficacy of a sensor can be assessed by examining the linearity of the fitting curves. A strong association between RI changes and sensor response is reflected by an increased slope of the curve fitting. Fig. 3e and f illustrate the fluctuation in resonance wavelength and the corresponding fitting curves for analyte RI ranging from 1.33 to 1.42. The table displays the parameters and results for the fourth-order fitting.

The adjusted R^2 values for the fitted curve of the resonance wavelengths are 0.99953 and 0.99907 for transverse polarization modes (x and y), respectively, very close to 1. This indicates that the designed sensor demonstrates exceptional sensing capabilities.

In all cases, a more defined peak profile with a greater confinement loss is achieved in the y-polarization mode. This indicates that the SPP mode operates more effectively, and the plasmonic resonance state is more prominent in y-polarization. Therefore, in subsequent investigations, we examine the sensor's y-polarization reliability.

Table 4 presents a comparative study of the designed D-shaped PCF-based SPR sensor's performance with existing published PCF-based SPR sensors, emphasizing the key characteristics such as AS, WS, R, and FoM. Our designed D-shaped sensor exhibits excellent performance compared to the other sensors, offering the maximum AS of 1178 per RIU, the highest WS of 20 000 nm per RIU, excellent wavelength resolution of 5×10^{-6} RIU, and a moderate FoM of 366 per RIU for y polarization mode. The aforementioned properties make the designed sensor exceptionally effective for accurate and precise RI detection.

3.2. Variation of architectural parameters

This section highlights the sensor functionality by modifying structural parameters. The RIs of 1.40 and 1.41 were selected as reference values to assess the sensor's performance under variations in geometric parameters. Subsequent investigations were carried out by adjusting these parameters while employing the selected RI values as benchmarks.

3.3. Influence of air hole diameters on sensor performance

In a PCF, the air holes act as the fundamental cladding zone. To enhance the sensor's sensitivity, the influence of geometric

Table 7 Evaluation of sensor performance for AS and WS over different analyte RI variations when the simulation uses only an Au layer and with a TiO_2 overlayer

	WS (nm per RIU)		AS (per RIU)		FoM (per RIU)	
Analyte RI	Au	Au + TiO_2	Au	Au + TiO_2	Au	Au + TiO_2
1.33	2000	2000	100	247	50	68
1.34	1000	3000	132	278	26	99
1.35	2000	3000	172	346	54	97
1.36	2000	3000	240	429	56	92
1.37	3000	5000	324	508	84	142
1.38	4000	6000	431	616	110	155
1.39	5000	7000	593	689	128	152
1.4	8000	12 000	758	836	179	215
1.41	12 000	20 000	987	1178	220	366
1.42						

parameters was investigated by simulating various air hole diameters (d_1, d_2). The initial assessment focused on the cladding air hole (d_1), as depicted in Fig. 1a. Fig. 4a demonstrates the loss peak of the structure for RIs of analyte ranging from n_a = 1.40 to n_a = 1.41. The data indicate that the loss peak increases as d_1 enlarges from 1.1 μm to 1.5 μm, as increasing the diameter of the smaller air hole enhances the refractive contrast between cladding and core, improving phase matching between the SPP and core mode. The findings indicate that deviations of d_1 from its optimal diameter alter the loss characteristics, thereby affecting the AS, as illustrated in Fig. 4b. Table 5 shows that variations in d_1 do not affect the resonance wavelength, caused by the strong confinement of the *y*-polarized mode within the core region. As indicated by Fig. 4a and b and Table 5, the sensor achieves its peak AS of 1178 per RIU at $d_1 = 1.1$ μm; therefore, this value was selected as the optimum diameter for the cladding small air hole.

Simulations were carried out for $d_2 = 3.5$, 3, 2.5 μm, with the outcomes displayed in Fig. 4c and d and Table 5. Fig. 4c shows that the peak loss for analyte RIs lies within the range of 1.40 to 1.41. The study indicates that the loss peak decreases as d_2 increases, and the loss peak exhibits an upward shift as d_2 decreases. The phenomenon occurs because of a bigger air hole diameter, which effectively confines the core-directed mode, keeping more of the light within the core and reducing interaction with the plasmonic film. As a result, the excitation of surface electrons weakens, lowering the evanescent wave's penetration and the overall confinement loss. A red shift is also observed with the increase in hole size. Fig. 4d presents the AS for $n_a = 1.40$ to $n_a = 1.41$. The overall best results were achieved at $d_2 = 3$ μm.

3.4. Influence of micro-channel on sensor efficacy

The integration of a micro-channel in a D-shaped PCF-based SPR sensor improves analyte accessibility and boosts the interaction between guided and SPP modes, resulting in increased resonance depth and sensitivity. Fig. 5a explains the effect of varying the micro-channel diameter. The micro-channel diameter increases from 6 μm to 8 μm in increments of 0.5 μm. At $r = 8$ μm, the confined loss escalates markedly from 106.88 dB cm^{-1} to 135.83 dB cm^{-1} as the RI changes from 1.40 to 1.41, indicating a pronounced sensitivity of loss to small RI shifts in this range. Fig. 5b illustrates that AS fluctuates considerably with changes in the value of *r*. The AS values for 6,

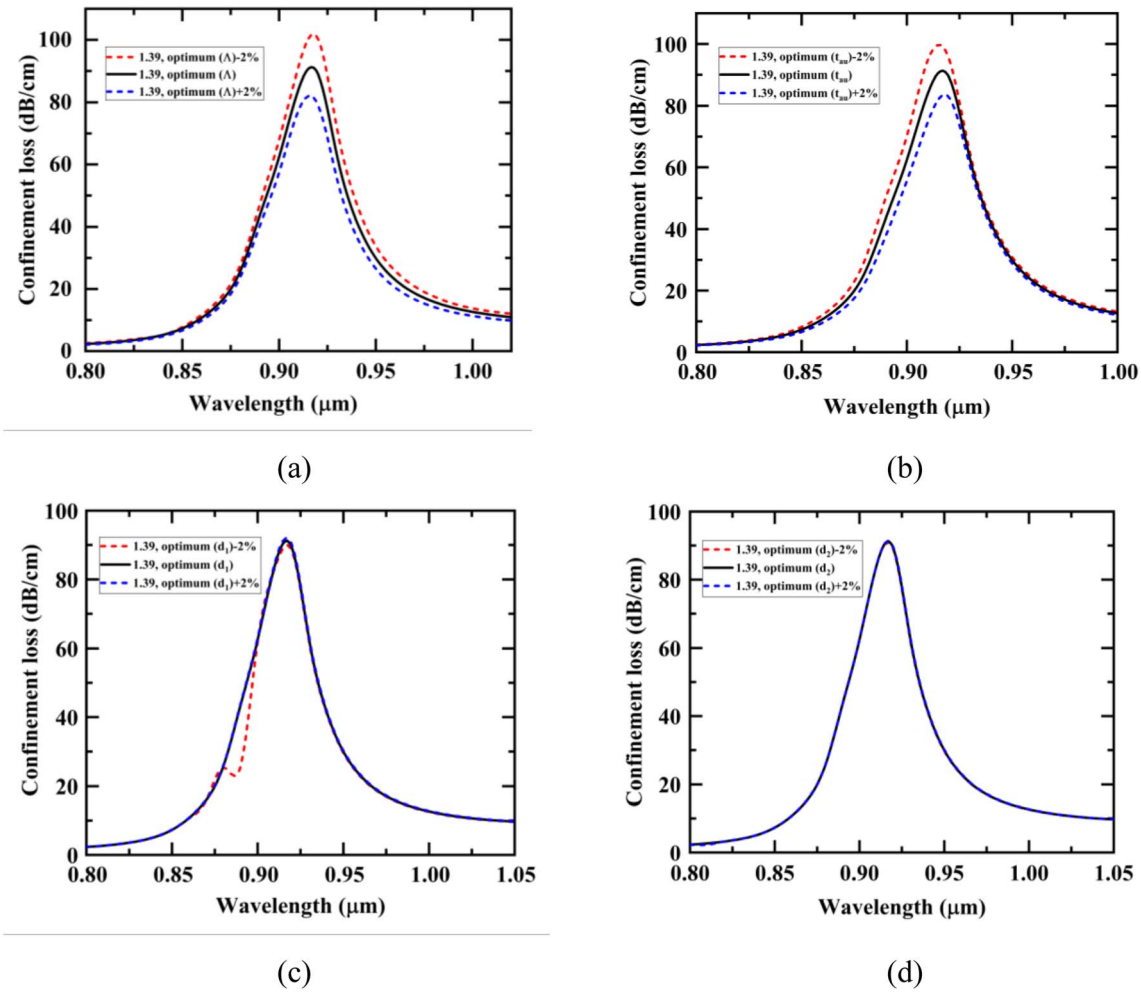

Fig. 8 Fabrication tolerance investigation for ±2% deviation of (a) pitch (Λ), (b) Au layer thickness (t_{au}), (c) diameter of air hole (d_1), and (d) diameter of air hole (d_2).

7, and 8 μm are 913, 958, and 1178 per RIU at n_a = 1.41, respectively. Thus, 8 μm is selected as the optimum microchannel diameter for the designed sensor. A detailed summary of the relationship between open channel diameter and sensor sensitivity is presented in Table 5.

3.5. Impact of pitch on sensor effectiveness

Pitch of the air holes influence the sensing efficacy of the sensor. In this study, the effect of the pitch variation is also investigated. To achieve optimal sensing performance, we precisely adjusted the pitch distance by gradually increasing it from 3.8 to 4.2 μm. Fig. 5c illustrates that the peak confinement loss is achieved at pitch = 3.8 μm, about 141.45 and 182.23 dB cm^{-1} for the analyte RI ranging from 1.40 to 1.41, respectively. As the distance increases, the peak loss decreases because the effective mode index differences between the cladding and core increase. Fig. 5d depicts that the AS obtained for the pitch = 4 μm is higher than that of the pitch = 3.8 μm and 4.2 μm. The ASs of 875, 1178, and 848 per RIU are achieved for the pitch distances of 3.8, 4, and 4.2 μm, respectively, at n_a = 1.41. Hence, 4 μm is picked as the most efficient pitch distance for the designed sensor. A detailed summary of the relationship between pitch distance and sensor sensitivity is presented in Table 5.

3.6. Impact of gold (Au) coating depth on sensing efficacy

The Au layer height significantly influences the sensor's effectiveness, as it directly alters the resonance wavelength shift. This effect was assessed by examining variations in Au thickness. Fig. 6a indicates that while the field confinement reduces with increasing Au thickness, the resonance peak experiences only a minor shift towards higher wavelengths for analyte RIs n_a = 1.40 to n_a = 1.41. To investigate the contribution of Au layer height on the confinement loss and the AS, the Au layer height was adjusted between 50 and 60 nm. Observations show that the loss is higher at Au = 50 nm, and lower at Au = 60 nm for analyte RIs n_a = 1.40 to n_a = 1.41. Fig. 6b shows that the AS obtained for the 50 nm Au layer is higher than that of the 55 nm and 60 nm layers, whereas its WS is lower than that of the 55 nm layer. The 55 nm Au layer exhibits moderate confinement loss along with enhanced AS and WS. Thus, 55 nm is chosen as the optimum Au layer height for the designed sensor. A detailed summary of the correlation between Au layer thickness and AS is presented in Table 6.

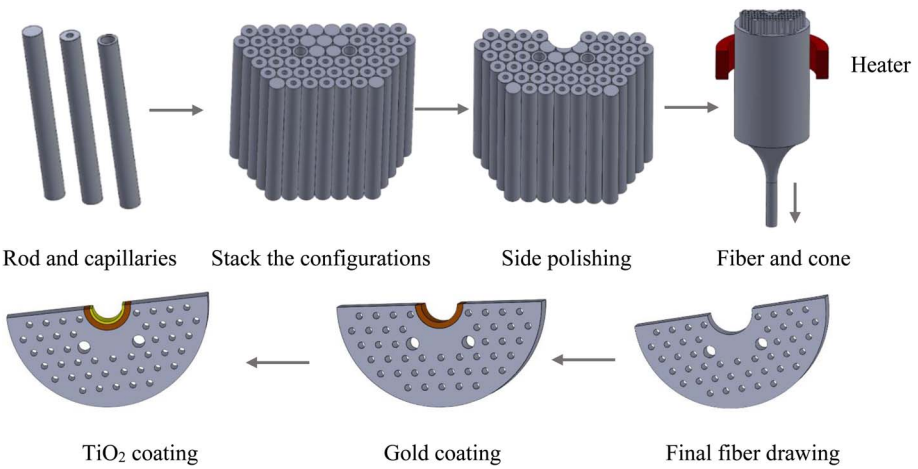

Fig. 9 Schematic of the designed sensor fabrication process.

Table 8 The RI variation for healthy cells and cancerous cells

		RI		
Cell name	Cell type and concentration level	Healthy cell	Cancerous cell	Ref.
Basal cell	(30–70%) Non-malignant cell (80%) Malignant skin lesion	1.360	1.380	45 and 46
HeLa	(30–70%) Non-malignant cell (80%) Cervical carcinoma	1.368	1.392	45 and 46
Jurkat	(30–70%) Non-malignant cell (80%) Blood malignancy	1.376	1.390	45 and 46
PC12	(30–70%) Non-malignant cell (80%) Adrenal carcinoma	1.381	1.395	46 and 47
MDA-MB-231	(30–70%) Non-malignant cell (80%) Mammary carcinoma	1.385	1.399	46 and 47
MCF-7	(30–70%) Non-malignant cell (80%) Mammary carcinoma	1.387	1.401	46 and 47

3.7. Impact of TiO_2 coating depth on sensing efficacy

A thin TiO_2 dielectric overlayer modifies the plasmon–analyte interaction by enhancing the propagation of the evanescent electromagnetic field into the analyte medium, thereby improving sensor sensitivity. The confinement loss curve and AS responses for different TiO_2 layer heights are explained in Fig. 6c and d. To evaluate the contribution of TiO_2 height on the sensing characteristics, the layer thickness was gradually changed from 10 to 8 nm for analyte RIs extending from 1.40 to 1.41. The observations show that the confinement loss is higher at TiO_2 = 10 nm than at TiO_2 = 9 nm and 8 nm as the RI changes. But a wavelength shift of 120 nm was seen in the loss spectrum peak with varying RIs at a height of 9 nm for TiO_2, as presented in Fig. 6c, yielding the peak WS of 12 000 nm per RIU. Fig. 6d indicates that the AS achieves its highest value of 1243 per RIU at a TiO_2 height of 10 nm, although its WS is

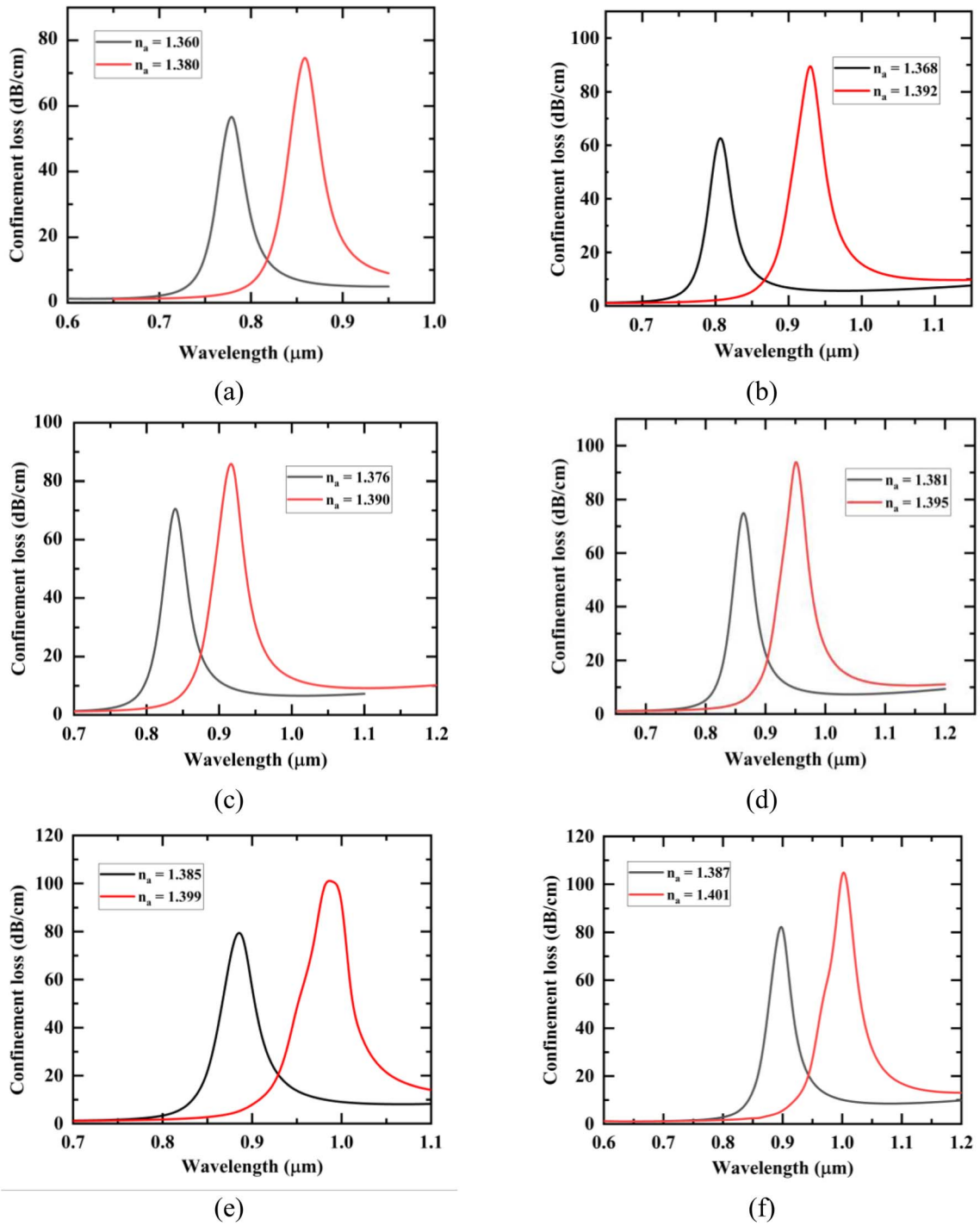

Fig. 10 (a–f) Outcomes of the identification of malignant skin lesions, cervical carcinoma, blood malignancy, adrenal carcinoma, and two variants of mammary carcinoma (MDA-MB-231 and MCF-7) utilizing the designed sensor, respectively.

comparatively lower than that of the 9 nm layer. The 9 nm TiO_2 layer exhibits an optimal trade-off between confinement loss and sensitivity enhancement, exhibiting both superior WS and AS with moderate confinement loss. Therefore, a TiO_2 layer height of 9 nm is identified as the efficient design parameter for the designed sensor. In Table 6, the correlation between the height of the TiO_2 layer and the associated sensing performance is summarized in detail.

3.8. Adding only gold coating

The simulation uses an Au layer without a TiO_2 overlayer. The findings are displayed in Fig. 7a and b and Table 7. Without an overlayer in the PCF-based SPR sensor design, the peak WS, AS, and FoM reached 12 000 nm per RIU, 987 per RIU, and 220 per RIU at $n_a = 1.41$, respectively. Although this shows moderate sensitivity, adding an overlayer further improved performance. The overlayer optimizes resonance by enhancing the connection between SPP and core guided modes, increasing sensitivity. After adding a TiO_2 overlayer, the sensor achieved the ultimate WS, AS, and FoM of 20 000 nm per RIU, 1178 per RIU, and 366 per RIU at $n_a = 1.41$, respectively. This underscores the importance of overlayers in refining the sensor's optical characteristics for better detection efficiency and sensitivity.

3.9. Investigation of fabrication tolerance

These tolerance variations represent practical uncertainties arising during micro-channel formation and Au/TiO_2 thin-film deposition in real fabrication processes. Despite the advancement in the fabrication process, there is still a statistical chance of an inevitable uncertainty that could alter the design variables from their optimal value. So, it is essential to analyze the design tolerance level of the suggested sensor. Therefore, within this segment, the analyte RI value 1.39 is chosen to assess the fabrication tolerance with ±2% variation of the sensor parameters. Fig. 8a illustrates the confinement loss curve due to ±2% variation of the pitch from its optimal value. With 2% decrease in the pitch from the optimal level, the loss increases, and with 2% increment, the loss decreases. However, shows no variation in the resonant wavelength of 920 nm in both cases. Fig. 8b shows that ± 2% variation in the Au film thickness (t_{au}) from its optimum value influences the loss curve. As demonstrated in Fig. 8b, the resonant wavelength remains unchanged at 920 nm, and confinement loss varies as the thickness changes by ±2% from its original value. The confinement loss grows from 89.21 to 95.17 dB cm^{-1}, by 2% decrease in gold thickness, and by 2% increase, loss decreases from 89.21 to 82.79 dB cm^{-1}. Furthermore, due to ±2% deviation of the air hole diameters d_1 and d_2, there is no significant movement in the loss curve, and the loss curve is almost identical, depicted in Fig. 8c and d, respectively. The resonant wavelength remains unchanged at 920 nm for analyte RI 1.39, with only minor variations in confinement loss. This confirms that the proposed sensor is highly robust against ±2% variations in structural parameters and that the simulated performance can be reliably translated to practical fabrication scenarios.

Despite the promising numerical performance, especially the sensitivity of the proposed sensor, certain limitations should be acknowledged. This study does not consider the effects of other practical factors, such as temperature variations, measurement noise, and spectral broadening, which are not included in the simulations. These aspects can be evaluated in future work.

3.10. Evaluation of the fabrication feasibility of the proposed PCF sensor

The fabrication viability of PCFs is investigated in this section, with a focus on the possibility of developing a particular fiber structure. Compared to conventional fibers, PCFs are more beneficial; several methods are utilized for the fabrication of the sensor, including stack-and-draw procedures, die-casting technique, and sol–gel processing.[40] The fabrication procedures for the micro-channel-based D-shaped sensor are demonstrated in Fig. 9a. Complex shapes such as circular, triangular, and square lattices can be easily created using the stack-and-draw procedure, which offers an extensible and versatile approach for the fabrication of PCFs. In this structure, thin and thick capillaries are employed to generate large and tiny air holes, wherein guiding cores are created by swapping a capillary with a solid rod and then removing these rods entirely.[41,42] After the fabrication of PCF, TiO_2, and Au layers on the PCF can be easily coated through various deposition techniques, such as the chemical vapor deposition method and atomic layer deposition (ALD).[43,44] The unidentified analyte can be detected by analyzing the confinement loss of the sensor.

3.11. Biomedical application

This segment presents the optical responses at different wavelengths for both non-malignant and diseased biological samples, incorporating six different carcinoma cell types, utilizing the refractive indices from Table 8. The performance of the D-shape PCF-based SPR sensor is shown in Fig. 10a–f for a variety of biological samples, such as Basal, HeLa, Jurkat, PC12, and mammary carcinoma cell types MDA-MB-231 and

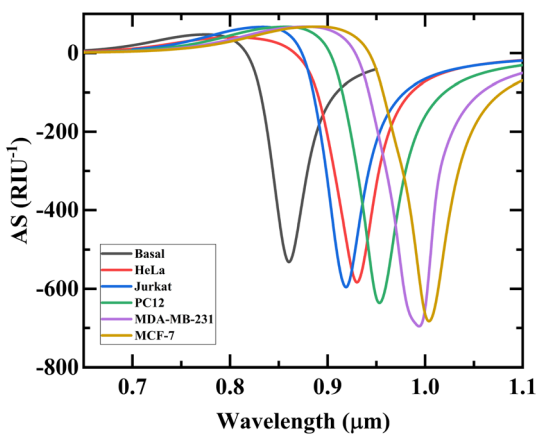

Fig. 11 AS for the following six carcinoma cell types: PC12, MDA-MB-231, Jurkat, HeLa, Basal, and MCF-7.

Table 9 Assessment of the sensor's effectiveness at refined design variables for identifying different carcinoma cell types

Cancer type	Cell type	WS (nm per RIU)	AS (per RIU)	FoM (per RIU)	Resolution (RIU)
Skin	Basal	4000.00	580.15	122.70	2.5×10^{-5}
Cervical	HeLa	5000.00	628.57	144.93	2.0×10^{-5}
Blood	Jurkat	5714.29	640.34	155.28	1.75×10^{-5}
Adrenal gland	PC12	6428.57	669.29	159.91	1.56×10^{-5}
Breast	MDA-MB-231	6428.57	717.29	153.06	1.56×10^{-5}
Breast	MCF-7	7142.86	708.02	165.34	1.40×10^{-5}

MCF-7. The red line in every scenario denotes malignant cells, whereas the black line shows normal (healthy) cells. The differences in RI, originating from cellular variations such as cytoplasmic density and membrane composition, produce distinct plasmonic resonance shifts, enabling clear discrimination between healthy and malignant cells.

In every scenario, carcinoma cells show higher confinement losses and redshifted resonance peaks in comparison to their normal counterparts. One of the most frequently employed means for assessing sensor efficacy is spectral interrogation, which is based on the variations in resonance peaks across the wavelength spectrum. This idea can be clarified by applying eqn (5), which examines wavelength changes associated with the loss peak and refractive index variations. Additionally, sensor effectiveness can be evaluated using the AS at a particular wavelength, as calculated using eqn (6). Based on the cancer cell types that were studied, the spectral sensitivities were 4000, 5000, 5714.29, 6428.57, 6428.57, and 7142.86 nm per RIU for Basal, HeLa, Jurkat, PC12, MDA-MB-231, and MCF-7 cells, while the corresponding ASs were 580.15, 628.57, 640.34, 669.29, 717.29, and 708.02 per RIU, respectively. Fig. 11 and Table 9 provide detailed information regarding the sensor's performance, including sensitivity, figure of merit (FoM), and resolution for six different types of carcinoma cells. The designed D-shaped sensor exhibits remarkable sensitivity, FoM, and resolution, signifying that this sensor delivers superior response. Moreover, in this study cancer cells detection are based on FEM simulations; experimental validation is the necessary next step to confirm the sensor's performance in real-world sample detection.

4. Conclusion

Accurate and early detection of cancer plays a vital role in enhancing patient outcomes, and non-invasive diagnostic techniques are making significant advances to address this issue. Among various non-invasive optical tools, D-shaped PCF-based SPR sensors are at the forefront due to their excellent sensitivity and fabrication simplicity. This study has designed a PCF-based SPR sensor for the identification of various carcinoma cells utilizing a D-shaped structure. The spectral and amplitude interrogation methods have been employed to investigate the performance of the proposed sensor. The impact of incorporating multiple air holes and their size, diameter, pitch distance, along with the impact of adding a plasmonic layer, TiO_2 overlayer, and their thickness on sensor performance has been comprehensively analyzed to obtain the optimized structure. The sensor achieved the highest AS and WS of 717.29 per RIU and 7142.86 nm per RIU, respectively, recorded for MDA-MB-231 and MCF-7 cells. Additionally, the designed sensor exhibited the highest spectral sensitivity of 20 000 nm per RIU across the RI span of 1.330 to 1.420 for *y*-polarized light. The sensor also depicted outstanding FoM, AS, and resolution values of 366 per RIU, 1178 per RIU, and 5×10^{-6} RIU, respectively, within the aforementioned RI range. Finally, a convenient and effective way of the presented sensor's fabrication is proposed with a detailed analysis of fabrication feasibility *via* investigating its fabrication tolerance. The outcomes of the simulation show an impressive improvement in sensitivity and accuracy compared to the state-of-the-art studies in the literature, which is a testament that the designed architecture could be an effective tool for the precise diagnosis of cancer with better resolution. It should be emphasized that all analyses, including cancer-cell detection and fabrication-tolerance evaluation, are carried out through FEM simulations; experimental validation is required to confirm the sensor's performance in real biological environments.

Author contributions

Kazi Zannatul Ferdwushee: writing – original draft, software, formal analysis, methodology, visualization. Md Abu Shahid Chowdhury: conceptualization, supervision, writing – original draft, formal analysis, validation, visualization. Siddika Tamanna Islam: writing – review & editing.

Conflicts of interest

The authors declare they have no conflicts of interests.

Data availability

The data that support the findings of this study will be made available from the corresponding author upon reasonable request.

References

1 M. A. Huraiya, S. G. Ramaraj, Sk. Md. Shahadat Hossain, K. Chakrabarti, H. Tabata and S. M. A. Razzak, A highly

optimized and sensitive bowtie shape-based SPR biosensor for different analyte detection, *Nanoscale Adv.*, 2025, **7**(3), 899–908, DOI: 10.1039/D4NA00812J.

2 W. Zhu, *et al.*, High confidence plasmonic sensor based on photonic crystal fibers with a U-shaped detection channel, *Phys. Chem. Chem. Phys.*, 2023, **25**(12), 8583–8591, DOI: 10.1039/D2CP04605A.

3 W. Zhu, *et al.*, Highly sensitive plasmonic sensor based on eccentric-core photonic crystal fibers, *Phys. Chem. Chem. Phys.*, 2023, **25**(29), 19596–19605, DOI: 10.1039/D3CP01615C.

4 R. L. Siegel, T. B. Kratzer, A. N. Giaquinto, H. Sung and A. Jemal, Cancer statistics, 2025, *Ca-Cancer J. Clin.*, 2025, **75**(1), 10–45, DOI: 10.3322/caac.21871.

5 A. Saha, M. T. Rahman and B. Dey, A high-performance BaTiO3/Ag/BP-based plasmonic biosensor for label-free detection of cancer biomarkers, *Sens. Actuators Phys.*, 2025, **396**, 117121, DOI: 10.1016/j.sna.2025.117121.

6 F. Bray, *et al.*, Global cancer statistics 2022: GLOBOCAN estimates of incidence and mortality worldwide for 36 cancers in 185 countries, *Ca-Cancer J. Clin.*, 2024, **74**(3), 229–263, DOI: 10.3322/caac.21834.

7 H. M. Rai and J. Yoo, A comprehensive analysis of recent advancements in cancer detection using machine learning and deep learning models for improved diagnostics, *J. Cancer Res. Clin. Oncol.*, 2023, **149**(15), 14365–14408, DOI: 10.1007/s00432-023-05216-w.

8 A. Thamilselvan and M. I. Kim, Recent advances on nanozyme-based electrochemical biosensors for cancer biomarker detection, *TrAC, Trends Anal. Chem.*, 2024, **177**, 117815, DOI: 10.1016/j.trac.2024.117815.

9 V. S. P. K. S. A. Jayanthi, A. B. Das and U. Saxena, Recent advances in biosensor development for the detection of cancer biomarkers, *Biosens. Bioelectron.*, 2017, **91**, 15–23, DOI: 10.1016/j.bios.2016.12.014.

10 S. Kumar and R. Singh, Recent optical sensing technologies for the detection of various biomolecules: Review, *Opt. Laser Technol.*, 2021, **134**, 106620, DOI: 10.1016/j.optlastec.2020.106620.

11 R. Zhang, J. Jiang and W. Wu, Wearable chemical sensors based on 2D materials for healthcare applications, *Nanoscale*, 2023, **15**(7), 3079–3105, DOI: 10.1039/D2NR05447G.

12 A. S. Chowdhury, Md. A. Islam, Md. S. Islam, B. Dey and J. Park, Design and Analysis of $PtSe_2$ and Blue Phosphorus/MoS_2 Heterostructure-Based SPR Biosensor, *ACS Appl. Opt. Mater.*, 2024, **2**(6), 1046–1059, DOI: 10.1021/acsaom.4c00050.

13 A. Khodaie and H. Heidarzadeh, Ultra-sensitive surface plasmon resonance sensor integrating MXene (Ti3C2TX) and graphene for advanced carcinoembryonic antigen detection, *Sci. Rep.*, 2025, **15**(1), 13571, DOI: 10.1038/s41598-025-97853-z.

14 A. K. Sharma, R. Jha and B. D. Gupta, Fiber-Optic Sensors Based on Surface Plasmon Resonance: A Comprehensive Review, *IEEE Sens. J.*, 2007, **7**(8), 1118–1129, DOI: 10.1109/JSEN.2007.897946.

15 A. Ramola, A. K. Shakya, A. Droby and A. Bergman, Numerical Study of a Novel Kagome-Inspired Photonic Crystal Fiber-Based Surface Plasmon Resonance Biosensor for Detection of Blood Components and Analytical Targets, *Biosensors*, 2025, **15**(8), 539, DOI: 10.3390/bios15080539.

16 A. Ramola, A. K. Shakya, A. Vidyarthi, S. Singh, E. Talker, and A. Bergman, Next-generation photonic-crystal-fiber-based plasmonic sensor for heavy metal detection *via* spectroscopy and refractive index integration, in *29th International Conference on Optical Fiber Sensors*, ed. M. Lopez-Amo Sainz, J. L. Santos, and T. Sun, SPIE, Porto, Portugal, 2025, p. 489, DOI: 10.1117/12.3062891.

17 A. Ramola, A. K. Shakya and A. Bergman, Comprehensive Analysis of Advancement in Optical Biosensing Techniques for Early Detection of Cancerous Cells, *Biosensors*, 2025, **15**(5), 292, DOI: 10.3390/bios15050292.

18 A. Ramola, A. K. Shakya, V. Kumar and A. Bergman, Recent Advances in Photonic Crystal Fiber-Based SPR Biosensors: Design Strategies, Plasmonic Materials, and Applications, *Micromachines*, 2025, **16**(7), 747, DOI: 10.3390/mi16070747.

19 A. Ramola, A. K. Shakya and A. Bergman, Finite Element Method-Based Modeling of a Novel Square Photonic Crystal Fiber Surface Plasmon Resonance Sensor with a Au–TiO2 Interface and the Relevance of Artificial Intelligence Techniques in Sensor Optimization, *Photonics*, 2025, **12**(6), 565, DOI: 10.3390/photonics12060565.

20 M. Ashrafian, S. Olyaee and M. Seifouri, Highly sensitive cancer detection using an open D-channel PCF-based SPR biosensor, *Sci. Rep.*, 2025, **15**(1), 10168, DOI: 10.1038/s41598-025-95249-7.

21 J. M. Nijhum and T. Ahmed, Highly sensitive quasi-D-shaped photonic crystal fiber biosensor designed for the detection of RBC parasitized by Plasmodium falciparum for the early diagnosis of malaria, *Opt. Continuum*, 2023, **2**(6), 1315, DOI: 10.1364/OPTCON.489682.

22 J. Divya, S. Selvendran, A. S. Raja and V. Borra, A Novel Plasmonic Sensor Based on Dual-Channel D-Shaped Photonic Crystal Fiber for Enhanced Sensitivity in Simultaneous Detection of Different Analytes, *IEEE Trans. NanoBiosci.*, 2024, **23**(1), 127–139, DOI: 10.1109/TNB.2023.3294330.

23 D. Zhou, F. Ren, Y. Li, Y. Ci and J. Wang, A Broadband D-Shaped Photonic Crystal Fiber Sensor *via* Surface Plasmon Resonance for Different Analytes with a Large Range of Refractive Index Detection, *Plasmonics*, 2024, **20**(4), 1991–2001, DOI: 10.1007/s11468-024-02425-y.

24 A. Oudenani and A. Sonne, A D-Shaped SPR-Based PCF Biosensor with a High Sensitivity for Wide Refractive Index Detection, *Plasmonics*, 2024, **20**(7), 5245–5253, DOI: 10.1007/s11468-024-02689-4.

25 M. Azadi, M. Seifouri, S. Olyaee and M. Mohammadi, Ultrahigh-sensitivity D-shaped PCF-SPR biosensor with TiO2–Au hybrid layers for precise detection of blood constituents, *Results Phys.*, 2025, **77**, 108463, DOI: 10.1016/j.rinp.2025.108463.

26 A. Vial, A.-S. Grimault, D. Macías, D. Barchiesi and M. L. De La Chapelle, Improved analytical fit of gold dispersion:

Application to the modeling of extinction spectra with a finite-difference time-domain method, *Phys. Rev. B*, 2005, **71**(8), 085416, DOI: 10.1103/PhysRevB.71.085416.

27 J. R. DeVore, Refractive Indices of Rutile and Sphalerite, *J. Opt. Soc. Am.*, 1951, **41**(6), 416, DOI: 10.1364/JOSA.41.000416.

28 I. H. Malitson, Interspecimen Comparison of the Refractive Index of Fused Silica, *J. Opt. Soc. Am.*, 1965, **55**(10), 1205, DOI: 10.1364/JOSA.55.001205.

29 T. P. White, R. C. McPhedran, C. M. De Sterke, L. C. Botten and M. J. Steel, Confinement losses in microstructured optical fibers, *Opt. Lett.*, 2001, **26**(21), 1660, DOI: 10.1364/OL.26.001660.

30 A. A. Rifat, G. A. Mahdiraji, Y. M. Sua, R. Ahmed, Y. G. Shee and F. R. M. Adikan, Highly sensitive multi-core flat fiber surface plasmon resonance refractive index sensor, *Opt. Express*, 2016, **24**(3), 2485, DOI: 10.1364/OE.24.002485.

31 M. Hautakorpi, M. Mattinen and H. Ludvigsen, Surface-plasmon-resonance sensor based on three-hole microstructured optical fiber, *Opt. Express*, 2008, **16**(12), 8427, DOI: 10.1364/OE.16.008427.

32 Md. A. Mollah, S. M. R. Islam, Md. Yousufali, L. F. Abdulrazak, Mb. B. Hossain and I. S. Amiri, Plasmonic temperature sensor using D-shaped photonic crystal fiber, *Results Phys.*, 2020, **16**, 102966, DOI: 10.1016/j.rinp.2020.102966.

33 M. Hautakorpi, M. Mattinen and H. Ludvigsen, Surface-plasmon-resonance sensor based on three-hole microstructured optical fiber, *Opt. Express*, 2008, **16**(12), 8427, DOI: 10.1364/OE.16.008427.

34 A. Aray, *et al.*, SPR-based plastic optical fibre biosensor for the detection of C-reactive protein in serum, *J. Biophotonics*, 2016, **9**(10), 1077–1084, DOI: 10.1002/jbio.201500315.

35 A. K. Yetisen, *et al.*, Color-Selective 2.5D Holograms on Large-Area Flexible Substrates for Sensing and Multilevel Security, *Adv. Opt. Mater.*, 2016, **4**(10), 1589–1600, DOI: 10.1002/adom.201600162.

36 J. Divya, S. Selvendran, A. S. Raja and V. Borra, A Novel Plasmonic Sensor Based on Dual-Channel D-Shaped Photonic Crystal Fiber for Enhanced Sensitivity in Simultaneous Detection of Different Analytes, *IEEE Trans. NanoBiosci.*, 2024, **23**(1), 127–139, DOI: 10.1109/TNB.2023.3294330.

37 D. Zhou, F. Ren, Y. Li, Y. Ci and J. Wang, A Broadband D-Shaped Photonic Crystal Fiber Sensor *via* Surface Plasmon Resonance for Different Analytes with a Large Range of Refractive Index Detection, *Plasmonics*, 2024, **20**(4), 1991–2001, DOI: 10.1007/s11468-024-02425-y.

38 X. Lu, X. Yu, J. Zhou, M. Chang and D. Lu, An Ultra-Wide Range D-Shaped Fiber SPR Sensor with a Nanostructure of Gold–MoS2 and Sodium for the Simultaneous Measurement of Refractive Index and Temperature, *Sensors*, 2025, **25**(2), 377, DOI: 10.3390/s25020377.

39 S. Mittal, *et al.*, Design and Performance Analysis of a Novel Hoop-Cut SPR-PCF Sensor for High Sensitivity and Broad Range Sensing Applications, *IEEE Sens. J.*, 2024, **24**(3), 2697–2704, DOI: 10.1109/JSEN.2023.3339813.

40 D. Pysz, *et al.*, Stack and draw fabrication of soft glass microstructured fiber optics, *Bull. Pol. Acad. Sci.: Tech. Sci.*, 2014, **62**(4), 667–682, DOI: 10.2478/bpasts-2014-0073.

41 A. A. Rifat, F. Haider, R. Ahmed, G. A. Mahdiraji, F. R. Mahamd Adikan and A. E. Miroshnichenko, Highly sensitive selectively coated photonic crystal fiber-based plasmonic sensor, *Opt. Lett.*, 2018, **43**(4), 891, DOI: 10.1364/OL.43.000891.

42 D. J. J. Hu and H. P. Ho, Recent advances in plasmonic photonic crystal fibers: design, fabrication and applications, *Adv. Opt. Photonics*, 2017, **9**(2), 257, DOI: 10.1364/AOP.9.000257.

43 V. Cremers, R. L. Puurunen and J. Dendooven, Conformality in atomic layer deposition: Current status overview of analysis and modelling, *Appl. Phys. Rev.*, 2019, **6**(2), 021302, DOI: 10.1063/1.5060967.

44 Jyoti, *et al.*, Recent advances in Metal-Organic Framework-Based fiber optic sensors and Photodetectors: Synthesis, Properties, and applications, *Chem. Eng. J.*, 2025, **507**, 160543, DOI: 10.1016/j.cej.2025.160543.

45 X. J. Liang, A. Q. Liu, C. S. Lim, T. C. Ayi and P. H. Yap, Determining refractive index of single living cell using an integrated microchip, *Sens. Actuators Phys.*, 2007, **133**(2), 349–354, DOI: 10.1016/j.sna.2006.06.045.

46 M. Schürmann, J. Scholze, P. Müller, J. Guck and C. J. Chan, Cell nuclei have lower refractive index and mass density than cytoplasm, *J. Biophotonics*, 2016, **9**(10), 1068–1076, DOI: 10.1002/jbio.201500273.

47 A. Hossan, M. A. S. Chowdhury, S. T. Islam and K. Z. Ferdwushee, Design and optimization of an optical ring resonator based biosensor for cancer detection, *Discov. Electron.*, 2025, **2**(1), 50, DOI: 10.1007/s44291-025-00090-x.

